ACS APPLIED MATERIALS & INTERFACES

www.acsami.org

Research Article

Ultrasensitive Detection of Hydrogen Peroxide Using Bi_2Te_3 Electrochemical Sensors

Fujia Zhao, Shan Zhou, and Yingjie Zhang*

Cite This: *ACS Appl. Mater. Interfaces* 2021, 13, 4761−4767

Read Online

ACCESS | Metrics & More | Article Recommendations | Supporting Information

ABSTRACT: Electrochemical sensors, with high accuracy, good selectivity, and linear response, have been widely used for environmental protection, health monitoring, and disease treatment. However, to date, these sensors still have limit sensitivity or otherwise require the use of high-cost materials such as noble metals and enzymes. Here, we report a novel electrochemical sensor using a topological insulator, Bi_2Te_3. Through liquid-phase exfoliation, we prepared nano- and microflakes of Bi_2Te_3 and measured their performance in hydrogen peroxide sensing via electrocatalytic reduction processes. Our devices exhibit a sensitivity of ∼4900 μA mM^{-1} cm^{-2} and a detection limit of $\sim 10^{-8}$ molar, both of which are superior to typical noble metal-based electrochemical sensors. Through electrochemical analysis and microkinetic simulations, we extracted the kinetic parameters and gained insights into the reaction mechanism. We attribute the ultrahigh sensitivity to the facile electron transfer at the Bi_2Te_3−aqueous solution interface.

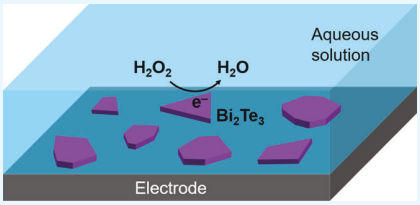

KEYWORDS: *hydrogen peroxide, electrochemical sensor, topological insulator, bismuth telluride, chemical and biosensing*

INTRODUCTION

Topological materials, including topological insulators and topological semimetals, are systems where strong spin−orbit coupling induces band inversion in the bulk and delocalized, topologically protected states on the surface.[1] While their band structure and electronic transport properties have been studied for over a decade, the past 2−3 years have seen a surge of interest in utilizing topological materials as catalysts to promote electrochemical reactions, such as hydrogen evolution, oxygen reduction/evolution, and CO_2 reduction.[2−9] High catalytic activities have been predicted via density functional theory calculations and observed experimentally. The superior performance was attributed to: (i) high carrier mobility of the topological surface states; (ii) topological protection and immunity of the surface states from chemical contaminations; and (iii) the surface states, derived from the sp band (in the case of bismuth chalcogenide topological insulators), are more delocalized than the typical d-bands in noble metals, thus facilitating surface diffusion of adsorbed molecules.[2−12] These properties are also ideal for electrochemical sensing since the highly mobile and delocalized surface states can facilitate interfacial charge transfer, while the topological protection can minimize the current noise induced by parasitic surface modifications; both factors lead to enhancement of the signal-to-noise ratio of the sensing current. However, to date, topological material-based electrochemical sensors have been rarely reported. While there have been a few studies of sensors based on Bi_2Se_3 hybridized with other binder materials,[13−15] it is not clear how the Bi_2Se_3 components contribute to the interfacial molecular binding and charge transfer processes, and their sensing performance is not on par with the noble metal-based sensors.

Hydrogen peroxide (H_2O_2) is an important chemical not only for industrial and everyday use as bleaches and disinfectants but also for regulating various metabolisms in biological systems such as cellular signaling, oxidative stress, aging, and cancer growth.[16−20] All of these biological functions depend sensitively on the intracellular concentration of H_2O_2, which typically ranges from 10 nM to 1 μM.[16,17] Therefore, sensitive detection of H_2O_2 in the nano- to micromolar range is critical for health monitoring and disease diagnosis. While enzyme-based electrochemical sensors have been developed and clinically used for H_2O_2 detection, their high cost and low thermal and chemical stability limit their large-scale production and diagnostic applications.[20−24] Therefore, tremendous efforts have been devoted to developing inorganic electrocatalysts for H_2O_2 detection in the past few years.[25−36] However, to date, most of the existing enzyme-free electrochemical sensors either require expensive precious metals or have limited sensitivity (Table 1 and Table S1, Supporting Information). Therefore, low-cost and highly sensitive H_2O_2 electrochemical sensors are urgently needed.

Received: November 7, 2020
Accepted: December 30, 2020
Published: January 14, 2021

Table 1. Comparison of the Performance of Various Reported H_2O_2 Sensors

Material	Sensitivity (μA mM^{-1} cm^{-2})	LOD (μM)	Ref.
CoO-CoS/NF	0.059	0.89	33
$NiCo_2O_4$ NSs	303.42	0.596	34
Au NPs/Cu-MOF	1710	1.2	28
Ag@MOF/GO	80.23	0.18	27
IE-MoS_2	1706	0.2	25
$ZnO/Co_3O_4/NiCo_2O_4$	388	0.163	29
PtNi/MWCNT	2123.1	0.06	35
CoO_x NPs/cholesterol oxidase	43.5	4.2	52
Ni_2P nanosheets	690.7	0.2	53
Co_3N NW/Ti	139.9	1	54
Nickel borate nanoarray	18,320	0.00085	55
Cu_3N NA/Cu	7600	0.0089	56
Fe_3N-Co_2N/carbon	2273.8	0.059	57
Bi_2Te_3	4903	0.016	this work

RESULTS AND DISCUSSION

Here, we report ultrasensitive H_2O_2 electrochemical sensors using topological insulator Bi_2Te_3 nano- and microflakes. To achieve both high crystalline quality and the exposure of surfaces, edges, and corners as potential active sites for H_2O_2 reduction, we used a facile liquid-phase exfoliation method for producing Bi_2Te_3 flakes by sonicating bulk powder samples (see the Methods section). From electron microscopy imaging, we found that the flakes have lateral sizes ranging from a few nanometers to a few microns (Figure 1a and Figure S1, Supporting Information), and the structure is crystalline consisting of quintuple layers as expected (Figure 1b). Elemental analysis from energy-dispersive X-ray spectroscopy (EDS) reveals homogeneous distribution of Bi and Te elements and a stoichiometric composition of the 2:3 Bi/Te ratio (Figure 1c and Figure S2). Using atomic force microscopy (AFM), we observed various morphologies of these flakes, where the exposed facets have different orientations, crystalline domains, and surface roughness (Figure 1d). The nanoscale thickness and rich surface structure of these flakes ensure both high conductivity and exposure of various possible active sites, thus facilitating electrochemical sensing.

The sensor performance was tested using a standard three-electrode electrochemical cell, where the working electrode consists of Bi_2Te_3 deposited on a glassy carbon electrode (see the Methods section for details). We first measured the linear sweep voltammetry (LSV) curves at different H_2O_2 concentrations from 0.3 to more than 30 μM. As shown in Figure 2a, clear reduction peaks are observed in all the curves, with a peak position between 0 and 0.1 V versus reversible hydrogen electrode (RHE). At a concentration higher than ~20 μM, a second peak emerges around 0.2 V versus RHE, which is likely due to the reduction of oxygen produced by H_2O_2 decomposition. To confirm that these peaks are not induced by the reduction of Bi_2Te_3, we performed LSV in the absence of H_2O_2 over a large potential range and found that the reduction of Bi_2Te_3 only occurs at a low potential of approximately −0.6 V versus RHE (Figure S3), in agreement with the previously reported Pourbaix diagram.[37] In addition, we performed control measurements of H_2O_2 sensing on a bare glassy carbon electrode (with no Bi_2Te_3) and observed negligible response (Figure S4). Therefore, we conclude that the observed peaks in Figure 2a are due to the reduction of H_2O_2 or other intermediates (e.g., O_2) catalyzed by the Bi_2Te_3 flakes.

We will focus on the main H_2O_2 reduction peak at ~0.05 V versus RHE in this study. The peak current density versus concentration shows a linear dependence (Figure 2b), revealing a sensitivity of ~4903 μA mM^{-1} cm^{-2} and a linear

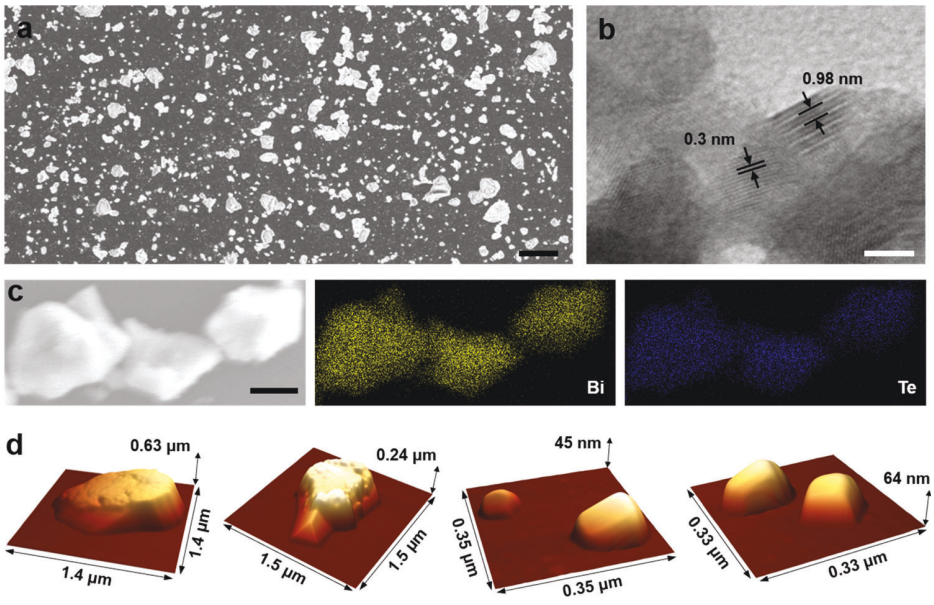

Figure 1. Structural characterization of Bi_2Te_3 flakes. (a) Scanning electron microscopy (SEM) image of the synthesized Bi_2Te_3 flakes. (b) Transmission electron microscopy (TEM) image showing the lattice structure of the flakes. (c) SEM image and EDS elemental mapping of a few Bi_2Te_3 flakes. (d) AFM images of different flakes in 3D view. Samples were drop-casted on silicon substrates for SEM and AFM imaging and on a copper grid for TEM imaging. Scale bars: 10 μm in panel (a), 4 nm in panel (b), and 2 μm in panel (c).

https://dx.doi.org/10.1021/acsami.0c19911
ACS Appl. Mater. Interfaces 2021, 13, 4761−4767

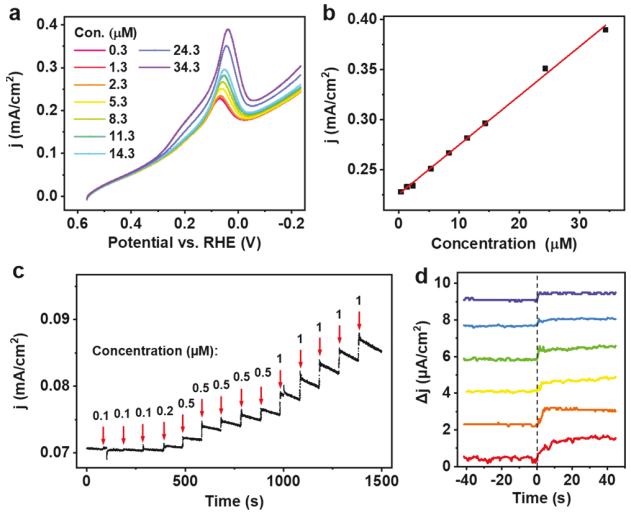

Figure 2. Performance of the electrochemical H_2O_2 sensor. (a) LSV curves at different H_2O_2 concentrations at a scan rate of 5 mV/s. (b) Peak current density as a function of H_2O_2 concentration. Black square dots and the red line show the raw data and linear fit, respectively. (c) CA response upon adding different amounts of H_2O_2 at a potential of 0.022 V vs RHE. (d) Expanded view of the step increase in current density when 0.1 μM H_2O_2 was added to different batches of sensor devices. The addition of H_2O_2 occurred at time = 0 s.

response throughout the measured range. To quantify the limit of detection (LOD), we measured the chronoamperometry (CA) response of the sensor upon adding small drops of H_2O_2 solutions at a fixed potential of 0.022 V versus RHE, which is close to the reduction peaks in the measured concentration range. As shown in Figure 2c, the device shows clear step increases of current density upon the addition of 0.1 μM H_2O_2, and the step height becomes larger when the amount of added H_2O_2 increases. Tests on different batches of sensors show similar responses upon the addition of 0.1 μM H_2O_2 (Figure 2d), revealing the reproducibility of these devices. Based on the CA results of different batches of samples, we also plotted the change of current density as a function of H_2O_2 concentration (Figure S5) and observed a linear response down to 0.1 μM. From the signal-to-noise (S/N) ratio of the step response, we extracted an LOD of 0.016 μM corresponding to S/N = 3. From Figure 2d, we can see that the response time of the sensor is typically within 2 s, which is mainly limited by the speed of the added H_2O_2 solution droplet mixing with the existing electrolyte, rather than an intrinsic response time of the sensor.

LSV measurements of a few different batches of sensor devices show similar performance, as summarized in Figure S6. All of the sensors exhibit linear response over the full tested range of 0.1−60 μM, and the actual linear range of the devices is likely larger. As summarized in Table 1 and Table S1, the sensitivity and LOD of our sensors are both among the best in all the reported devices. We have also measured LSV at different pH ranging from 5.5 to 8.5 and found that the sensitivity remains at similar values (Figure S7). In addition, our sensors show high selectivity for H_2O_2 detection over other species commonly found in physiological solutions, as shown in Figure S8. With high sensitivity, low detection limit, high selectivity, and low cost (inexpensive materials and device processing), our demonstrated Bi_2Te_3 sensors are promising for biosensing and clinical diagnosis applications.

Note that we used a low loading of ~0.05 mg/cm^2 for Bi_2Te_3 to fabricate the sensors. A further increase in loading only leads to a modest increase in current response (Figure S9), likely due to the Bi_2Te_3 flakes stacking on each other.

Previous studies of electrocatalysis using topological materials have used density functional theory (DFT) to calculate the electronic structure and adsorption energy and attributed the high catalytic activity to coupling of atomic active sites with the topological surface states, which can lead to favorable binding energies of the reactants.[7,8] While these thermodynamic properties are in general relevant to all types of electrochemical reactions, for sensing applications, the reaction kinetics is more critical, which directly impacts the magnitude of electrochemical current—the sensed signal in response to an analyte—at an optimized applied potential. To achieve sensitive detection of trace amounts of chemical species, it is important to have facile interfacial charge transfer to generate a large redox current. However, previous works on H_2O_2 electrochemical sensors have rarely reported on the analysis of the charge transfer rate constants. Therefore, a microkinetic analysis of our Bi_2Te_3-based electrochemical sensors will both be complementary to previous DFT simulations on the atomistic thermodynamics of the catalytic reactions and will shed light on the kinetics of the interfacial charge transfer processes.

To enable a thorough kinetic analysis, we performed cyclic voltammetry (CV) at different scan rates. As shown in Figure 3a, both cathodic (<0 V) and anodic peaks (>0.4 V) are observed. These CV results reveal that the H_2O_2 reduction reaction is in the quasi-reversible regime due to (i) the large anodic and cathodic peak separation and (ii) the shift of peak position at different scan rates. To quantify the kinetic parameters of H_2O_2 reduction, we extract the peak current density and peak potential as a function of the scan rate (ν), as shown in Figure 3b,c. The linear dependence of the peak current as a function of $\nu^{1/2}$ indicates that the reaction is diffusion-limited at a sufficiently negative potential.[38] The peak potential changes roughly linearly as a function of lnν, which is also expected for a quasi-reversible reaction as long as the scan rate is not too small.[38,39] We assume that the reaction proceeds via a two-electron reduction of H_2O_2

$$H_2O_2 + 2H^+ + 2e^- \rightarrow 2H_2O$$

To extract the standard rate constant, we use the following kinetic equation for the quasi-reversible reactions[38,39]

$$\Delta E = E_p - E_{1/2} = -\Xi(\Lambda, \alpha)\left(\frac{RT}{F}\right)$$

where E_p is the peak potential, $E_{1/2}$ is the half-wave potential (middle of the anodic and cathodic peaks), R is the ideal gas constant, T = 298 K is the temperature, and F is the Faraday constant. In addition, Λ is determined by $\Lambda = \frac{k^0}{(D_O^{1-\alpha} D_R^{\alpha} f\nu)^{1/2}}$, where k^0 is the standard rate constant of the reaction, D_O = 1.2 × 10^{-9} m^2/s and D_R = 2.3 × 10^{-9} m^2/s are the diffusion coefficients of H_2O_2 and H_2O molecules, respectively,[40,41] and $f = F/RT$. The transfer coefficient α can be determined from the ratio of the Tafel slope of the measured cathodic (slope$_c$) and anodic (slope$_a$) waves: $\frac{\text{slope}_c}{\text{slope}_a} = \frac{-\alpha}{1-\alpha}$. We obtain α = 0.51.

https://dx.doi.org/10.1021/acsami.0c19911
ACS Appl. Mater. Interfaces 2021, 13, 4761−4767

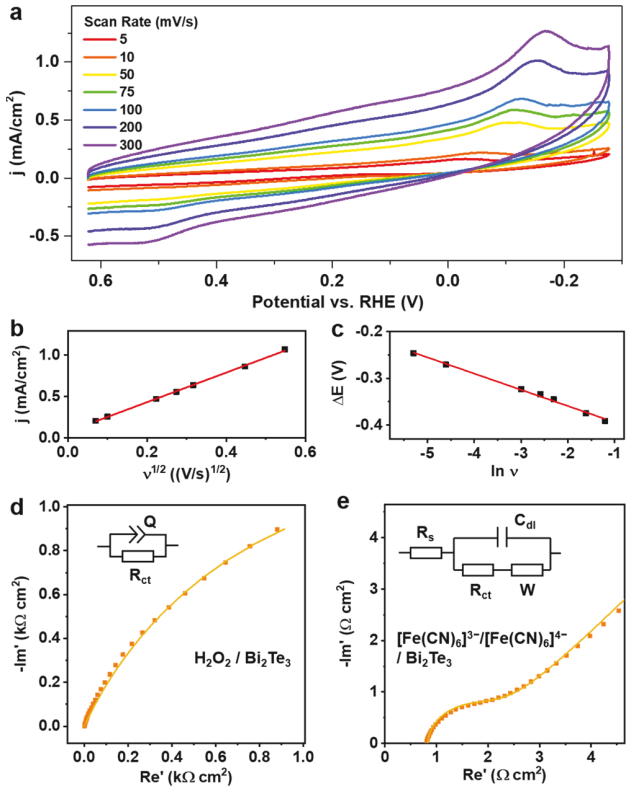

Figure 3. Kinetic analysis. (a) CV curves at different scan rates with a H_2O_2 concentration of 81 μM. (b) Cathodic peak current as a function of the square root of the scan rate, including the raw data and linear fit. (c) Linear regression of the cathodic peak position (relative to the half-wave potential) as a function of the natural logarithm of the scan rate (with a unit of V/s). (d) Nyquist plot of an EIS measurement of 100 μM H_2O_2 in 0.1 M K_2SO_4 solution at a potential of 0.066 V vs RHE. (e) EIS result of 5.0 mM $K_3Fe(CN)_6$ and 5.0 mM $K_4Fe(CN)_6$ in an aqueous solution containing 0.1 M K_2SO_4 at a standard potential of 0.764 V vs RHE. In both panels (d, e), dots and lines are the raw experimental data and the fitting results using the equivalent circuit models shown in the insets, respectively. The obtained values of the equivalent circuit elements are R_{ct} = 3.3 kΩ cm^2, $Q = 7.38 \times 10^{-4}$ Ω^{-1} s^n cm^{-2}, and phase factor n = 0.724 in panel (d) and R_{ct} = 1.2 Ω cm^2, solution resistance R_s = 0.83 Ω cm^2, double-layer capacitance C_{dl} = 188.7 μF/cm^2, and Warburg coefficient σ = 19.1 Ω s$^{-1/2}$ cm^2 in panel (e).

Ξ is a parameter that has a fixed dependence on Λ and α.[38,39] Substituting the experimental data and standard parameters into these formulas, we obtain $k^0 \approx 3 \times 10^{-5}$ cm/s. Note that k^0 is the rate constant at the half-wave potential. At other cathodic potentials (E), the reaction rate constant is $k = k^0 e^{-\alpha f(E - E_{1/2})}$. For example, at a scan rate of 5 mV/s, the cathodic peak potential occurs at $\Delta E = E_p - E_{1/2} \approx -0.25$ V, and the corresponding rate constant is $k \approx 4.3 \times 10^{-3}$ cm/s.

The kinetic parameters can also be determined independently from electrochemical impedance spectroscopy (EIS). Assuming that the kinetics follows the Butler–Volmer model, at cathodic potentials, we obtain $k = \frac{RT}{\alpha n F^2 C R_{ct}}$,[38] where R_{ct} is the charge transfer resistance, n = 2 is the charge transfer number, and C is the initial concentration of H_2O_2. We performed EIS measurements at C = 100 μM and E = 0.066 V versus RHE and obtained the Nyquist plot (Figure 3d). Using an RQ (parallel resistance and constant phase element) circuit model, we fit the EIS spectrum and obtain R_{ct} = 3.3 kΩ cm^2. Therefore, the rate constant can be obtained as $k = 7.9 \times 10^{-4}$ cm/s. The standard rate constant is thus $k^0 = k e^{\alpha f(E - E_{1/2})} = 3.6 \times 10^{-5}$ cm/s. We can see that the k^0 values obtained using these two methods are similar, confirming the validity of our kinetic analysis algorithms.

Previous studies on the rate constants of H_2O_2 reduction on different electrodes have reported a large range of values between 10^{-6} and 10^{-2} cm/s.[42−48] These values are measured at different electrode potentials and by using different techniques (LSV, CA, or rotating ring disk electrode measurements). As a result, it is not clear whether the obtained kinetic parameters can be directly compared. Our cross-validated kinetic analyses using two independent methods (CV and EIS) represent an important advancement for accurate determination of the H_2O_2 reduction kinetics. Further studies by using in situ characterization techniques (e.g., vibrational spectroscopy) may reveal the key atomistic reaction steps responsible for the obtained kinetic rate constants, although such measurements are beyond the scope of this work.

Given the complication of the H_2O_2 reduction processes, we resort to a standard redox couple, ferricyanide/ferrocyanide (5 mM each in 0.1 M K_2SO_4 solution), as a medium to compare the charge transfer resistance of our Bi_2Te_3 catalyst with other reported catalysts for H_2O_2 sensing. We performed EIS of this redox couple and extracted the Nyquist plot, as shown in Figure 3e. Using a Randles equivalent circuit model, we obtain an R_{ct} of 1.2 Ω cm^2. This is smaller than other catalyst materials typically used for H_2O_2 sensing (measured using the same redox couple), such as noble metal nanostructures, 2D materials and heterostructures, and oxide nanomaterials.[35,36,49−51] This result reveals that our Bi_2Te_3 catalysts have intrinsically facile interfacial charge transfer kinetics, which may be due to wave function delocalization of the topological surface states.

To further verify the kinetic parameters and understand the reaction mechanism, we performed microkinetic simulations based on the Butler–Volmer model[38] (see the Methods section for simulation details). Using the parameters extracted from experimental data, we simulated CV curves at a series of different H_2O_2 concentrations and scan rate parameters, as shown in Figure 4a,b. Except for double-layer capacitance and solution resistance effects that are not included in the simulation, the main features of the simulated CV curves are consistent with the experimental results, including the position, separation and asymmetry of the cathodic and anodic peaks, and the dependence of the peak intensity on H_2O_2 concentration and scan rate. These agreements reveal that

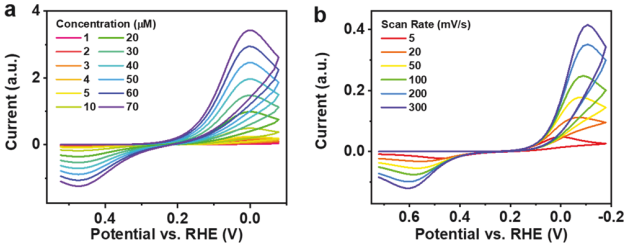

Figure 4. Microkinetic simulations. (a) CV at different H_2O_2 concentrations with a scan rate of 5 mV/s. (b) CV at different scan rates with a H_2O_2 concentration of 1 μM.

https://dx.doi.org/10.1021/acsami.0c19911
ACS Appl. Mater. Interfaces 2021, 13, 4761−4767

the reactions are indeed quasi-reversible and can be reasonably explained using the classical kinetics model. While this model does not contain the atomistic details of the interfacial charge transfer processes, it offers a general framework for understanding the electrochemical sensing properties based on the inherently sluggish redox reactions, such as the reduction of oxygen and H_2O_2.

CONCLUSIONS

In conclusion, we demonstrated an ultrasensitive electrochemical sensor for H_2O_2 detection using nanostructured topological insulators. Through microkinetic analysis and simulations, we found that facile interfacial charge transfer is likely the key factor leading to high sensitivity. We expect topological materials to be promising for applications in a large variety of chemical and biosensors.

METHODS

Materials Synthesis and Electrode Preparation. Commercial Bi_2Te_3 powders purchased from Sigma Aldrich were dispersed in DI water with a 1:1000 weight ratio. The mixture solution was then ultrasonicated in a Branson sonicator (M2800) for 24 h and stored as stock solution. To prepare each working electrode, 10 μL of sonicated solution was drop-casted onto a glassy carbon disk electrode (Pine E5TQ) and then dried in a N_2 atmosphere overnight. The geometric surface area of the electrode was 0.196 cm^2, and the surface coverage was estimated to be 7.9% from direct SEM imaging of the glassy carbon electrodes in multiple areas. As a result, we estimated an electrochemical surface area of ~0.0155 cm^2.

Electron Microscopy Characterization. For SEM, samples were prepared by drop casting Bi_2Te_3 flakes on Si substrates or glassy carbon electrode inserts and imaged using Hitachi S4700 and S4800 SEM. EDS mappings were obtained using an IXRF system integrated to Hitachi S4700 SEM. For TEM, samples were prepared by drop casting Bi_2Te_3 flakes on a Cu TEM grid and then imaged using JEOL 2100 Cryo TEM with a LaB_6 emitter at 200 kV.

Atomic Force Microscopy Characterization. AFM measurements were performed using Cypher ES AFM (Asylum Research, Oxford Instruments). Tap 300 Al-G probes purchased from Budget Sensors were used for AC mode imaging. Imaging parameters were optimized to ensure that the repulsive mode was reached[58,59] so that the obtained height profiles of the flakes were accurate.

Electrochemical Measurements. LSV, CV, CA, and EIS measurements were carried out using a standard three-electrode setup with one glassy carbon working electrode (Pine E5TQ), one Ag/AgCl reference electrode (BASi MF-2052), and one Pt counter electrode (CHI 115). The electrolyte was aqueous solutions of 0.1 M K_2SO_4, unless otherwise noted. To eliminate the dissolved oxygen in the solution, we purged the electrolyte using ultrapure argon for at least 1 h before the electrochemical measurements and continuously purged argon throughout all the electrochemical tests. We used a commercial dissolved oxygen sensor (Go Direct optical dissolved oxygen probe from Vernier) to monitor the oxygen content during argon purging and found that the concentration reached a low level of ~0.52 mg/L and remained constant throughout the electrochemical tests (Figure S10). LSV and CV were carried out using a CHI 600E potentiostat (CH Instruments). EIS was measured using either a CHI 760 potentiostat from CH Instruments or a VSP potentiostat from BioLogic. In the beginning of the electrochemical measurements, we usually perform LSV down to −0.278 V versus RHE to activate the Bi_2Te_3 catalyst (likely due to the removal of the surface oxide layer) before measuring the H_2O_2 reduction reactions. The electrolyte used in EIS measurements was either 100 μM H_2O_2 in 0.1 M K_2SO_4 or a mixture of 5.0 mM $K_3Fe(CN)_6$ and 5.0 mM $K_4Fe(CN)_6$ dissolved in 0.1 M K_2SO_4 solution. All the electrochemical measurements were carried out with either no electrode rotation or with a rotation speed of 200 rpm. When the electrode was not rotated, a magnetic stir bar was used with a stirring rate of 800 rpm.

Kinetic Simulation. The simulation of CV curves followed the finite difference method proposed by Britz.[60] Mass transfer was determined by Fick's law, and the reaction current was determined by the Butler−Volmer equation. The input parameters were the rate constant, charge transfer coefficient, scan rate, and initial concentration of H_2O_2, all of which were the same as or close to the experimental values.

ASSOCIATED CONTENT

Supporting Information

The Supporting Information is available free of charge at https://pubs.acs.org/doi/10.1021/acsami.0c19911.

SEM images of individual Bi_2Te_3 flakes, EDS spectrum of a Bi_2Te_3 flake, LSV of the Bi_2Te_3 / glassy carbon electrode in the absence of H_2O_2, LSV of bare glassy carbon electrode, Change of current density vs H_2O_2 concentration extracted from CA measurements, LSV results of different batches of H_2O_2 sensors at pH=5.5 and other pH values, selectivity test of the sensor, LSV measurements with different Bi_2Te_3 loadings, concentration of dissolved oxygen during continuous argon purging, and performance of other reported H_2O_2 electrochemical sensors (Figures S1−S10 and Table S1) (PDF)

AUTHOR INFORMATION

Corresponding Author

Yingjie Zhang − *Department of Materials Science and Engineering and Materials Research Laboratory, University of Illinois, Urbana, Illinois 61801, United States;* orcid.org/0000-0002-2704-8894; Email: yjz@illinois.edu

Authors

Fujia Zhao − *Department of Materials Science and Engineering and Materials Research Laboratory, University of Illinois, Urbana, Illinois 61801, United States*

Shan Zhou − *Department of Materials Science and Engineering and Materials Research Laboratory, University of Illinois, Urbana, Illinois 61801, United States;* orcid.org/0000-0002-6476-3280

Complete contact information is available at: https://pubs.acs.org/10.1021/acsami.0c19911

Notes

The authors declare no competing financial interest.

https://dx.doi.org/10.1021/acsami.0c19911
ACS Appl. Mater. Interfaces 2021, 13, 4761−4767

■ ACKNOWLEDGMENTS

This work was supported by the University of Illinois at Urbana-Champaign. The experiments were carried out in part in the Materials Research Laboratory Central Facilities and in the Carl R. Woese Institute for Genomic Biology at the University of Illinois. The authors acknowledge the use of facilities and instrumentation supported by NSF through the University of Illinois Materials Research Science and Engineering Center DMR-1720633.

■ REFERENCES

(1) Vergniory, M. G.; Elcoro, L.; Felser, C.; Regnault, N.; Bernevig, B. A.; Wang, Z. A Complete Catalogue of High-Quality Topological Materials. *Nature* **2019**, *566*, 480−485.
(2) Yang, Q.; Li, G.; Manna, K.; Fan, F.; Felser, C.; Sun, Y. Topological Engineering of Pt-Group-Metal-Based Chiral Crystals toward High-Efficiency Hydrogen Evolution Catalysts. *Adv. Mater.* **2020**, *32*, 1908518.
(3) Li, G.; Fu, C.; Shi, W.; Jiao, L.; Wu, J.; Yang, Q.; Saha, R.; Kamminga, M. E.; Srivastava, A. K.; Liu, E.; Yazdani, A. N.; Kumar, N.; Zhang, J.; Blake, G. R.; Liu, X.; Fahlman, M.; Wirth, S.; Auffermann, G.; Gooth, J.; Parkin, S.; Madhavan, V.; Feng, X.; Sun, Y.; Felser, C. Dirac Nodal Arc Semimetal $PtSn_4$: An Ideal Platform for Understanding Surface Properties and Catalysis for Hydrogen Evolution. *Angew. Chem., Int. Ed.* **2019**, *58*, 13107−13112.
(4) Li, J.; Ma, H.; Xie, Q.; Feng, S.; Ullah, S.; Li, R.; Dong, J.; Li, D.; Li, Y.; Chen, X.-Q. Topological Quantum Catalyst: Dirac Nodal Line States and a Potential Electrocatalyst of Hydrogen Evolution in the TiSi Family. *Sci. China Mater.* **2018**, *61*, 23−29.
(5) Zhang, N.; Zheng, F.; Huang, B.; Ji, Y.; Shao, Q.; Li, Y.; Xiao, X.; Huang, X. Exploring Bi_2Te_3 Nanoplates as Versatile Catalysts for Electrochemical Reduction of Small Molecules. *Adv. Mater.* **2020**, *32*, 1906477.
(6) Rajamathi, C. R.; Gupta, U.; Kumar, N.; Yang, H.; Sun, Y.; Süß, V.; Shekhar, C.; Schmidt, M.; Blumtritt, H.; Werner, P.; Yan, B.; Parkin, S.; Felser, C.; Rao, C. N. R. Weyl Semimetals as Hydrogen Evolution Catalysts. *Adv. Mater.* **2017**, *29*, 1606202.
(7) Qu, Q.; Liu, B.; Liang, J.; Li, H.; Wang, J.; Pan, D.; Sou, I. K. Expediting Hydrogen Evolution through Topological Surface States on Bi_2Te_3. *ACS Catal.* **2020**, *10*, 2656−2666.
(8) Li, G.; Xu, Q.; Shi, W.; Fu, C.; Jiao, L.; Kamminga, M. E.; Yu, M.; Tüysüz, H.; Kumar, N.; Süß, V.; Saha, R.; Srivastava, A. K.; Wirth, S.; Auffermann, G.; Gooth, J.; Parkin, S.; Sun, Y.; Liu, E.; Felser, C. Surface States in Bulk Single Crystal of Topological Semimetal $Co_3Sn_2S_2$ toward Water Oxidation. *Sci. Adv.* **2019**, *5*, No. eaaw9867.
(9) Li, L.; Zeng, J.; Qin, W.; Cui, P.; Zhang, Z. Tuning the Hydrogen Activation Reactivity on Topological Insulator Heterostructures. *Nano Energy* **2019**, *58*, 40−46.
(10) Memmel, N.; Bertel, E. Role of Surface States for the Epitaxial Growth on Metal Surfaces. *Phys. Rev. Lett.* **1995**, *75*, 485−488.
(11) Chen, H.; Zhu, W.; Xiao, D.; Zhang, Z. CO Oxidation Facilitated by Robust Surface States on Au-Covered Topological Insulators. *Phys. Rev. Lett.* **2011**, *107*, No. 056804.
(12) Li, G.; Felser, C. Heterogeneous Catalysis at the Surface of Topological Materials. *Appl. Phys. Lett.* **2020**, *116*, 070501.
(13) Wu, S.; Liu, G.; Li, P.; Liu, H.; Xu, H. A High-Sensitive and Fast-Fabricated Glucose Biosensor Based on Prussian Blue/Topological Insulator Bi_2Se_3 Hybrid Film. *Biosens. Bioelectron.* **2012**, *38*, 289−294.
(14) Chen, S.; Fang, Y.-M.; Li, J.; Sun, J.-J.; Chen, G.-N.; Yang, H.-H. Study on the Electrochemical Catalytic Properties of the Topological Insulator Bi_2Se_3. *Biosens. Bioelectron.* **2013**, *46*, 171−174.
(15) Dong, S.; Li, M.; Wei, W.; Liu, D.; Huang, T. An Convenient Strategy for IgG Electrochemical Immunosensor: The Platform of Topological Insulator Materials Bi_2Se_3 and Ionic Liquid. *J. Solid State Electrochem.* **2017**, *21*, 793−801.
(16) Giorgio, M.; Trinei, M.; Migliaccio, E.; Pelicci, P. G. Hydrogen Peroxide: A Metabolic By-Product or a Common Mediator of Ageing Signals? *Nat. Rev. Mol. Cell Biol.* **2007**, *8*, 722−728.
(17) Sies, H. Role of Metabolic H_2O_2 Generation: Redox Signaling and Oxidative Stress. *J. Biol. Chem.* **2014**, *289*, 8735−8741.
(18) Yang, B.; Chen, Y.; Shi, J. Reactive Oxygen Species (ROS)-Based Nanomedicine. *Chem. Rev.* **2019**, *119*, 4881−4985.
(19) López-Lázaro, M. Dual Role of Hydrogen Peroxide in Cancer: Possible Relevance to Cancer Chemoprevention and Therapy. *Cancer Lett.* **2007**, *252*, 1−8.
(20) Veal, E. A.; Day, A. M.; Morgan, B. A. Hydrogen Peroxide Sensing and Signaling. *Mol. Cell* **2007**, *26*, 1−14.
(21) Chen, W.; Cai, S.; Ren, Q.-Q.; Wen, W.; Zhao, Y.-D. Recent Advances in Electrochemical Sensing for Hydrogen Peroxide: A Review. *Analyst* **2012**, *137*, 49−58.
(22) Tatsuma, T.; Ogawa, T.; Sato, R.; Oyama, N. Peroxidase-Incorporated Sulfonated Polyaniline−Polycation Complexes for Electrochemical Sensing of H_2O_2. *J. Electroanal. Chem.* **2001**, *501*, 180−185.
(23) Rhee, S. G.; Woo, H. A.; Kil, I. S.; Bae, S. H. Peroxiredoxin Functions as a Peroxidase and a Regulator and Sensor of Local Peroxides. *J. Biol. Chem.* **2012**, *287*, 4403−4410.
(24) Rhee, S. G.; Woo, H. A. Multiple Functions of Peroxiredoxins: Peroxidases, Sensors and Regulators of the Intracellular Messenger H_2O_2, and Protein Chaperones. *Antioxid. Redox Signaling* **2011**, *15*, 781−794.
(25) Shu, Y.; Zhang, W.; Cai, H.; Yang, Y.; Yu, X.; Gao, Q. Expanding the Interlayers of Molybdenum Disulfide toward the Highly Sensitive Sensing of Hydrogen Peroxide. *Nanoscale* **2019**, *11*, 6644−6653.
(26) Li, Y.; Zhang, P.; Ouyang, Z.; Zhang, M.; Lin, Z.; Li, J.; Su, Z.; Wei, G. Nanoscale Graphene Doped with Highly Dispersed Silver Nanoparticles: Quick Synthesis, Facile Fabrication of 3D Membrane-Modified Electrode, and Super Performance for Electrochemical Sensing. *Adv. Funct. Mater.* **2016**, *26*, 2122−2134.
(27) Li, C.; Wu, R.; Zou, J.; Zhang, T.; Zhang, S.; Zhang, Z.; Hu, X.; Yan, Y.; Ling, X. MNPs@anionic MOFs/ERGO with the Size Selectivity for the Electrochemical Determination of H_2O_2 Released from Living Cells. *Biosens. Bioelectron.* **2018**, *116*, 81−88.
(28) Dang, W.; Sun, Y.; Jiao, H.; Xu, L.; Lin, M. AuNPs-NH_2/Cu-MOF Modified Glassy Carbon Electrode as Enzyme-Free Electrochemical Sensor Detecting H_2O_2. *J. Electroanal. Chem.* **2020**, *856*, 113592.
(29) Xue, B.; Li, K.; Gu, S.; Zhang, L.; Lu, J. Ni Foam-Supported ZnO Nanowires and Co_3O_4/$NiCo_2O_4$ Double-Shelled Nanocages for Efficient Hydrogen Peroxide Detection. *Sens. Actuators, B* **2018**, *262*, 828−836.
(30) Zhu, L.; Zhang, Y.; Xu, P.; Wen, W.; Li, X.; Xu, J. PtW/MoS_2 Hybrid Nanocomposite for Electrochemical Sensing of H_2O_2 Released from Living Cells. *Biosens. Bioelectron.* **2016**, *80*, 601−606.
(31) Liu, J.; Bo, X.; Zhao, Z.; Guo, L. Highly Exposed Pt Nanoparticles Supported on Porous Graphene for Electrochemical Detection of Hydrogen Peroxide in Living Cells. *Biosens. Bioelectron.* **2015**, *74*, 71−77.
(32) Liu, M.; Liu, R.; Chen, W. Graphene Wrapped Cu_2O Nanocubes: Non-Enzymatic Electrochemical Sensors for the Detection of Glucose and Hydrogen Peroxide with Enhanced Stability. *Biosens. Bioelectron.* **2013**, *45*, 206−212.
(33) Mai, L. N. T.; Bui, Q. B.; Bach, L. G.; Nhac-Vu, H.-T. A Novel Nanohybrid of Cobalt Oxide-Sulfide Nanosheets Deposited Three-Dimensional Foam as Efficient Sensor for Hydrogen Peroxide Detection. *J. Electroanal. Chem.* **2020**, *857*, 113757.
(34) Chen, D.; Pang, D.; Zhang, S.; Song, H.; Zhu, W.; Zhu, J. Synergistic Coupling of $NiCo_2O_4$ Nanorods onto Porous Co_3O_4 Nanosheet Surface for Tri-Functional Glucose, Hydrogen-Peroxide Sensors and Supercapacitor. *Electrochim. Acta* **2020**, *330*, 135326.
(35) Mei, H.; Wu, H.; Wu, W.; Wang, S.; Xia, Q. Ultrasensitive Electrochemical Assay of Hydrogen Peroxide and Glucose Based on

https://dx.doi.org/10.1021/acsami.0c19911
ACS Appl. Mater. Interfaces 2021, 13, 4761−4767

PtNi Alloy Decorated MWCNTs. *RSC Adv.* **2015**, *5*, 102877−102884.
(36) Dong, S.; Yang, Q.; Peng, L.; Fang, Y.; Huang, T. Dendritic Ag@Cu Bimetallic Interface for Enhanced Electrochemical Responses on Glucose and Hydrogen Peroxide. *Sens. Actuators, B* **2016**, *232*, 375−382.
(37) Martín González, M. S.; Prieto, A. L.; Gronsky, R.; Sands, T.; Stacy, A. M. Insights into the Electrodeposition of Bi_2Te_3. *J. Electrochem. Soc.* **2002**, *149*, C546.
(38) Bard, A. J.; Faulkner, L. R. *Electrochemical Methods: Fundamentals and Applications*; 2nd ed.; Wiley: New York, 2001.
(39) Matsuda, H.; Ayabe, Y. Zur Theorie Der Randles-Sevčikschen Kathodenstrahl-Polarographie. *Zeitschrift für Elektrochemie, Berichte der Bunsengesellschaft für Phys. Chemie* **1955**, *59*, 494−503.
(40) Schumb, W. C.; Satterfield, C. N.; Wentworth, R. L. *Hydrogen Peroxide (American Chemical Society Monograph Series. No. 128.)*; Reinhold Publishing Corporation: New York, 1955.
(41) Mills, R. Self-Diffusion in Normal and Heavy Water in the Range 1-45.Deg. *J. Phys. Chem.* **1973**, *77*, 685−688.
(42) Patra, S.; Munichandraiah, N. Electrochemical Reduction of Hydrogen Peroxide on Stainless Steel. *J. Chem. Sci.* **2009**, *121*, 675.
(43) Wu, Y.; Muthukrishnan, A.; Nagata, S.; Nabae, Y. Kinetic Understanding of the Reduction of Oxygen to Hydrogen Peroxide over an N-Doped Carbon Electrocatalyst. *J. Phys. Chem. C* **2019**, *123*, 4590−4596.
(44) Parimi, N. S.; Umasankar, Y.; Atanassov, P.; Ramasamy, R. P. Kinetic and Mechanistic Parameters of Laccase Catalyzed Direct Electrochemical Oxygen Reduction Reaction. *ACS Catal.* **2012**, *2*, 38−44.
(45) Wu, J.; Zhang, D.; Niwa, H.; Harada, Y.; Oshima, M.; Ofuchi, H.; Nabae, Y.; Okajima, T.; Ohsaka, T. Enhancement in Kinetics of the Oxygen Reduction Reaction on a Nitrogen-Doped Carbon Catalyst by Introduction of Iron via Electrochemical Methods. *Langmuir* **2015**, *31*, 5529−5536.
(46) Muthukrishnan, A.; Nabae, Y. Estimation of the Inherent Kinetic Parameters for Oxygen Reduction over a Pt-Free Cathode Catalyst by Resolving the Quasi-Four-Electron Reduction. *J. Phys. Chem. C* **2016**, *120*, 22515−22525.
(47) Jirkovský, J. S.; Halasa, M.; Schiffrin, D. J. Kinetics of Electrocatalytic Reduction of Oxygen and Hydrogen Peroxide on Dispersed Gold Nanoparticles. *Phys. Chem. Chem. Phys.* **2010**, *12*, 8042−8052.
(48) Rojas, M. I.; Andreussi, O.; Gomez, C. G.; Avalle, L. B. Kinetics and Mechanism of the Hydrogen Peroxide Reduction Reaction on a Graphite Carbon Nitride Sensor. *J. Phys. Chem. C* **2019**, *124*, 336−346.
(49) Song, H.; Ni, Y.; Kokot, S. Investigations of an Electrochemical Platform Based on the Layered MoS_2-Graphene and Horseradish Peroxidase Nanocomposite for Direct Electrochemistry and Electrocatalysis. *Biosens. Bioelectron.* **2014**, *56*, 137−143.
(50) Li, X.; Du, X. Molybdenum Disulfide Nanosheets Supported Au-Pd Bimetallic Nanoparticles for Non-Enzymatic Electrochemical Sensing of Hydrogen Peroxide and Glucose. *Sens. Actuators, B* **2017**, *239*, 536−543.
(51) Dong, S.; Xi, J.; Wu, Y.; Liu, H.; Fu, C.; Liu, H.; Xiao, F. High Loading MnO_2 Nanowires on Graphene Paper: Facile Electrochemical Synthesis and Use as Flexible Electrode for Tracking Hydrogen Peroxide Secretion in Live Cells. *Anal. Chim. Acta* **2015**, *853*, 200−206.
(52) Salimi, A.; Hallaj, R.; Soltanian, S. Fabrication of a Sensitive Cholesterol Biosensor Based on Cobalt-Oxide Nanostructures Electrodeposited onto Glassy Carbon Electrode. *Electroanalysis* **2009**, *21*, 2693−2700.
(53) Xiong, X.; You, C.; Cao, X.; Pang, L.; Kong, R.; Sun, X. Ni_2P Nanosheets Array as a Novel Electrochemical Catalyst Electrode for Non-Enzymatic H_2O_2 Sensing. *Electrochim. Acta* **2017**, *253*, 517−521.
(54) Xie, F.; Cao, X.; Qu, F.; Asiri, A. M.; Sun, X. Cobalt Nitride Nanowire Array as an Efficient Electrochemical Sensor for Glucose and H_2O_2 Detection. *Sens. Actuators, B* **2018**, *255*, 1254−1261.
(55) Wang, Z.; Xie, F.; Liu, Z.; Du, G.; Asiri, A. M.; Sun, X. High-Performance Non-Enzyme Hydrogen Peroxide Detection in Neutral Solution: Using a Nickel Borate Nanoarray as a 3D Electrochemical Sensor. *Chem. − A Eur. J.* **2017**, *23*, 16179−16183.
(56) Wang, Z.; Cao, X.; Liu, D.; Hao, S.; Kong, R.; Du, G.; Asiri, A. M.; Sun, X. Copper-Nitride Nanowires Array: An Efficient Dual-Functional Catalyst Electrode for Sensitive and Selective Non-Enzymatic Glucose and Hydrogen Peroxide Sensing. *Chem. − A Eur. J.* **2017**, *23*, 4986−4989.
(57) Zhou, D.; Cao, X.; Wang, Z.; Hao, S.; Hou, X.; Qu, F.; Du, G.; Asiri, A. M.; Zheng, C.; Sun, X. Fe_3N-Co_2N Nanowires Array: A Non-Noble-Metal Bifunctional Catalyst Electrode for High-Performance Glucose Oxidation and H2O2 Reduction toward Non-Enzymatic Sensing Applications. *Chem. − A Eur. J.* **2017**, *23*, 5214−5218.
(58) Panse, K. S.; Zhou, S.; Zhang, Y. 3D Mapping of the Structural Transitions in Wrinkled 2D Membranes: Implications for Reconfigurable Electronics, Memristors, and Bioelectronic Interfaces. *ACS Appl. Nano Mater.* **2019**, *2*, 5779−5786.
(59) Zhou, S.; Panse, K. S.; Motevaselian, M. H.; Aluru, N. R.; Zhang, Y. Three-Dimensional Molecular Mapping of Ionic Liquids at Electrified Interfaces. *ACS Nano* **2020**, *14*, 17515−17523.
(60) Britz, D.; Strutwolf, J. *Digital Simulation in Electrochemistry*; 3rd ed.; Springer: Berlin, Heidelberg, 2005, DOI: 10.1007/b97996.

https://dx.doi.org/10.1021/acsami.0c19911
ACS Appl. Mater. Interfaces 2021, 13, 4761−4767